Tidal response of seismic wave velocity at shallow crust in Japan

Tomoya Takano[1] and Kiwamu Nishida[2]

[1]Hirosaki University
[2]Earthquake Research Institute, University of Tokyo

February 9, 2023

Abstract

Microcracks in geomaterials cause variations in the elastic moduli under applied strain, thereby creating seismic wave velocity variations. These are crucial for understanding the dynamic processes of the crust, such as fault-zone damage, healing, and volcanic activities. Solid earth tides have been used to detect seismic velocity changes responding to crustal-scale deformations. However, no prior research has explored the characteristics of the seismic velocity variations caused by large-scale tidal deformation. To systematically evaluate the tidal response to velocity variations, we developed a new method that utilized the flexibility of a state-space model. The tidal response was derived from hourly stacked noise autocorrelations using a seismic interferometry method throughout Japan. In particular, large tide-induced seismic velocities were observed in the low S-wave velocity region of the shallow crust. Overall, the tidal responses to velocity variations can provide new insights into the response mechanisms of the shallow crust to applied strain.

Tidal response of seismic wave velocity at shallow crust in Japan

Tomoya Takano[1] and Kiwamu Nishida[2]

[1]Graduate School of Science and Technology, Hirosaki University
[2]Earthquake Research Institute, the University of Tokyo

Key Points:

- The spatial distribution of seismic velocity changes caused by tides was determined using dense network of seismic stations in Japan.
- The tidal response to velocity changes was extracted from ambient noise using an extended Kalman filter with a Maximum Likelihood method.
- Strain–velocity sensitivities tend to increase at a low S-wave velocity in the shallow crust.

Corresponding author: Tomoya Takano, `takanot@hirosaki-u.ac.jp`

Abstract

Microcracks in geomaterials cause variations in the elastic moduli under applied strain, thereby creating seismic wave velocity variations. These are crucial for understanding the dynamic processes of the crust, such as fault-zone damage, healing, and volcanic activities. Solid earth tides have been used to detect seismic velocity changes responding to crustal-scale deformations. However, no prior research has explored the characteristics of the seismic velocity variations caused by large-scale tidal deformation. To systematically evaluate the tidal response to velocity variations, we developed a new method that utilized the flexibility of a state-space model. The tidal response was derived from hourly stacked noise autocorrelations using a seismic interferometry method throughout Japan. In particular, large tide-induced seismic velocities were observed in the low S-wave velocity region of the shallow crust. Overall, the tidal responses to velocity variations can provide new insights into the response mechanisms of the shallow crust to applied strain.

Plain Language Summary

Rock deformations can open or close microcracks in rocks along with varying their elastic moduli under an applied strain. The temporal variations in the elastic moduli of rocks alter the seismic wave velocity, which can be monitored to provide information on the strain applied to the crust. This is crucial for understanding the geological processes in the fault zones and volcanic regions. To utilize the seismic velocity variations for monitoring how much the Earth's structure deforms, the response of the seismic velocity to the deformations must be assessed. The deformation of the Earth's surface caused by the gravity of the Moon and Sun, which is called solid Earth tides, has been used to study seismic velocity variations in response to crustal deformation. However, only a limited number of regions have been studied for the tidal response of the seismic velocity, and the characteristics of its variations caused by tidal deformation were not yet apparent. This study measured the tidal responses to seismic velocity variations throughout Japan with reliable estimations. Notably, the tide-induced seismic velocity variations tend to increase in the low S-wave velocity region. Overall, these results provide new insights into the response mechanisms of the shallow crust to deformations.

1 Introduction

The temporal evolution of the stress or strain applied to the crust provides essential information for understanding the dynamic processes in fault zones and active volcanoes. This is because the occurrence of earthquakes depends on the stress or strain state of the Earth and the fluid distribution around the fault. Volcanic eruptions occur because of the pressure accumulation under volcanic fluid pressurization and magma supply from deeper regions. Upon observing the response of the crust to the applied stress or strain, the in-situ stress or strain variations in the crust can be estimated, which generally involve limitations in the case of direct measurement. The geomaterials in the crust are nonlinearly elastic (Walsh, 1965), and their elastic moduli vary with the applied strain. As the seismic wave velocity depends on the elastic moduli, the applied strain induces variations in the seismic wave velocity. Therefore, tracking the seismic wave velocity variations can adequately serve as a proxy for examining the temporal variations in the elastic constants caused by the applied strain in the crust. Previous studies have reported that the temporal variations in the seismic wave velocity are associated with the static strain variations induced by, for instance, large earthquakes (e.g. Brenguier, Campillo, et al., 2008) and volcanic activities (e.g. Brenguier, Shapiro, et al., 2008; Takano et al., 2017). To monitor the applied strain in the crust and its responses, the variations in the seismic wave velocity response to a given strain perturbation must be examined.

As we can precisely compute the static strain caused by a solid earth tide, the seismic velocity variations associated with the tidal strain provide information on the strain–velocity relationships on Earth. Earlier, in controlled active seismic experiments, the seismic velocity observably varied with the tidal strain (e.g. De Fazio et al., 1973; Reasenberg & Aki, 1974; Yamamura et al., 2003). However, active seismic experiments do not yield temporal resolution and constrained locations in repeated experiments. Recently, a passive noise-based technique (e.g. Obermann & Hillers, 2019) observed seismic velocity variations related to tides (e.g. Takano et al., 2014, 2019; Sens-Schönfelder & Eulenfeld, 2019; Hillers et al., 2015; Mao et al., 2019). To estimate the velocity variations caused by tides, two strategies have been employed using ambient noise correlations. The first one involves the stacking of ambient noise correlations according to the tidal deformation amplitude and measuring the phase differences between the noise correlations during the dilatation and contraction of the crust (Takano et al., 2014; Hillers et al., 2015; Takano et al., 2019). After stacking the noise correlations for a long time period, the velocity variations caused by the nontidal effects can be canceled. The second one examines the velocity variations corresponding to the tidal harmonics from the spectrum of seismic velocity variations with high temporal sampling (Sens-Schönfelder & Eulenfeld, 2019). These previous studies estimated the strain–velocity sensitivities based on the velocity variations induced by tidal deformation at depths shallower than a few kilometers. As such, the estimated magnitudes of strain–velocity sensitivity may depend on the strength of nonlinear elasticity at their location. Previous studies have employed several methods to detect the tidal responses of velocity variations and the spatial sensitivities of wavefields. The tidal responses to velocity variations have been detected in certain regions. However, no existing research has reported the spatial features of the seismic velocity variations observed in response to crustal-scale deformation. In order to estimate the spatial distribution of velocity changes in response to tides, it is necessary to measure the response using a uniform method and establish criteria for determining whether the seismic wave velocity responds to tides. This study aims to calculate the tidal response of the velocity variations in the shallow crust throughout Japan for proposing the criteria for detecting these tidal responses.

To estimate the variations in only seismic velocity related to tidal strain, the tidal response to the velocity variations must be accurately separated from the other causes of seismic velocity variations. Recently, Nishida et al. (2020) developed a novel method for estimating the seismic velocity variations using an extended Kalman filter based on a state-space model (e.g. Durbin & Koopman, 2012). They utilized an extended Kalman filter algorithm to estimate the seismic velocity variations as a state variable and used the Maximum Likelihood method to estimate the hyperparameters describing the velocity variations related to precipitation and large earthquakes. The flexibility of the state-space model for the time-series data can easily incorporate the seismic wave velocity variations induced by external perturbations into the model. As the period, phase, and amplitude of the tides were accurately determined in advance, the superposition of the periodic functions can model the tide-induced velocity variations. Thus, the tidal responses to the velocity variations were incorporated into the state-space model as hyperparameters to systematically estimate the tidal strain response using the extended Kalman filter and Maximum Likelihood method.

In this study, we investigated the seismic velocity variations in response to tidal strains throughout Japan. First, the nine components of the ambient-noise autocorrelation functions were calculated using Japan's dense seismic network. Thereafter, we extracted the seismic velocity variations related to the tide from the hourly stacked-noise correlation functions using an extended Kalman filter with a Maximum Likelihood method. The observed strain–velocity sensitivities were compared with the S-wave velocity structure at each station. The spatial distribution of the tide-induced velocity variations was studied to characterize the mechanical properties of the shallow crust in response to deformation. As the tides and seismic ambient noise can be observed at any location and instant, the flexibility of the state-space model will enable us to attain a higher spatial resolution of the tidal strain–velocity sensitivities with a dense seismic network, such as a Large N-array or Distributed Acoustic Sensing (DAS) observation.

2 Data

To detect the tidal response of seismic wave velocity variations, we computed the autocorrelation functions of ambient noise at a single station using 796 Hi-net seismic stations operated by the National Research Institute for Earth Science and Disaster Prevention (NIED). As most of the Hi-net network stations include the same borehole-type sensors, the characteristics among instruments will vary less. The location map of the seismic stations with the maximum tidal volumetric strain at the ground surface computed by GOTIC2 (Matsumoto et al., 2001) is illustrated in Figure 1. GOTIC2 computes the tidal strain, including the solid earth tide and ocean load. In the GOTIC2 program, ocean loading was computed with a five-minute resolution around Japan. The NIED deployed three-component velocity meters with a natural frequency of 1 Hz at the bottom of each borehole located at a depth of about 100 m or more at most stations. After subtracting the common data logger noise (Takagi et al., 2015), the instrumental responses of the seismometers were deconvolved using the inverse filtering technique (Maeda et al., 2011). We resampled the data to 2 Hz to efficiently compute the correlation functions. For each station every hour, we computed three components (north–north, east–east, upward–upward) of an auto-correlation function and six components (east–north, east–upward, north–east, north–upward, upward–east, and upward–north) of a single-station cross-correlation (Hobiger et al., 2014). The correlation functions were filtered at frequency bands of 0.2–0.5 Hz. In summary, we analyzed the ambient noise recorded from January 1, 2010, to December 31, 2011.

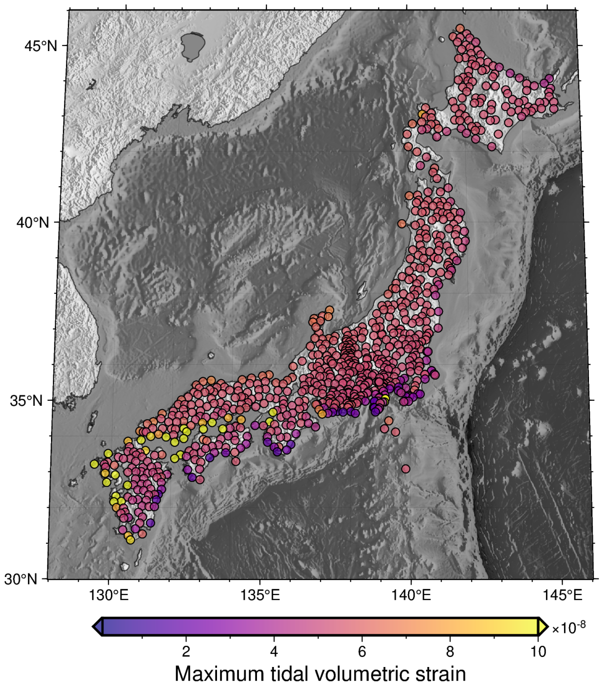

Figure 1. Location map of seismic stations. The color scale displays the maximum volumetric tidal strain during the observation period.

3 Method

The tidal response of seismic velocity variations was determined from the hourly stacked noise correlations using the extended Kalman filter with the Maximum Likelihood method based on the state-space model (Nishida et al., 2020). In Kalman filter processing, we minimized the squared differences between the model correlation function predicted from one previous step and the observed correlations. Assuming that the temporal variations of the seismic wave velocity in a given medium occur homogeneously, a model function of the observed correlations can be expressed by altering the amplitude and stretching factor of the reference correlation function using a stretching method in the time domain (Weaver & Lobkis, 2000). The stretching method has been linearized for application to a Kalman filter (Nishida et al., 2020). The tidal response of the velocity variations was determined as the explanatory variables in a state-space model in two steps. First, the temporal variations of amplitude and the stretching factor of the correlations were estimated as state variables in a state-space model with Kalman Filter processing. Second, the tidal response to the velocity variations was determined as an explanatory variable, referred to as a hyperparameter, using the Maximum Likelihood method. Thus, we constructed a state-space model as follows:

$$\boldsymbol{y}_t^p = \boldsymbol{m}^p \left(\boldsymbol{\alpha}_t + \boldsymbol{R}_t\right) + \boldsymbol{\epsilon}_t, \qquad \boldsymbol{\epsilon}_t \sim \mathcal{N}\left(0, \boldsymbol{H}_t\right) \tag{1}$$

$$\boldsymbol{\alpha}_{t+1} = \boldsymbol{\alpha}_t + \boldsymbol{\eta}_t, \qquad \boldsymbol{\eta}_t \sim \mathcal{N}\left(0, \boldsymbol{Q}_t\right), \tag{2}$$

where $\boldsymbol{y}_t^p$ denotes the data vector of the observed correlations for the p th component, $\boldsymbol{\alpha}_t$ represents the state vector, $\boldsymbol{R}_t$ symbolizes the explanatory variable related to the tides, and $\boldsymbol{\epsilon}_t$ and $\boldsymbol{\eta}_t$ indicate the mutually independent random variables subject to a normal distribution ($\mathcal{N}$) with zero means and covariance matrix $\boldsymbol{H_t}$ and $\boldsymbol{Q_t}$, respectively. The equations 1 and 2 have been elaborately expressed in the supplemental information (refer to Text S1).

To compute the reference correlation at each station, we first estimated the state variables of the stretching factor and amplitude common across all nine components without any explanatory variables. Thereafter, the reference correlation was estimated by averaging the observed correlations stretched with the estimated amplitude and stretching factor for the observation duration. Prior data covariance, h_0, was estimated based on the time average of the squared differences between the observed and reference correlations. The validation of prior data covariance is described in the supplemental information (Text S2). The state variables were estimated through the recursive linear Kalman filter and smoother (Durbin & Koopman, 2012) by adjusting the explanatory variables, initial stretching factor, and prior model covariance for the initial value.

The tidal response of the seismic wave velocity was modeled by adding the cosine functions related to the tidal constituents as follows:

$$r_t = \sum_{m=1}^{M} A_m \cos\left(\omega_m t + \varphi_m + \theta_m\right) \tag{3}$$

where m denotes the index of the tidal constituents, A_m indicates the sensitivity of the seismic wave velocity to tidal strain, φ_m represents the phase angle of the tide, ω_m denotes the angular frequency of the tide, and θ_m represents the difference between the tidal strain and the observed variations in seismic velocity. A phase delay may occur in the response of the velocity variations to tidal strain caused by the nonlinear elasticity of the rock (Sens-Schönfelder & Eulenfeld, 2019). φ_m was estimated from the theoretical tidal strain computed using GOTIC2 at each station, whereas ω_m was obtained from the table of tidal constituents (Cartwright & Edden, 1973). The velocity variations related to only M_2 tide were incorporated into the modeled tidal response of the seismic wave velocity, which most significantly contributed to the seismic wave velocity variations in the tidal constituents (Sens-Schönfelder & Eulenfeld, 2019). As the M_2 tide originated from the moon, the thermoelastic effects did not contribute to the seismic velocity variations.

The logarithmic likelihood $\ln L$ was maximized with respect to the hyperparameters. $\ln L$ was computed following the Kalman filtering processes (e.g. Durbin & Koopman, 2012); $\ln L$ is a function of hyperparameter β as

$$\beta = (p_0, p_1, \gamma_1, A_{M_2}, \varphi_{M_2}), \tag{4}$$

where p_0 and p_1 represent the covariance of the initial value of the amplitude and stretching factor, respectively, γ_1 denotes the initial value of the stretching factor, and A_{M_2} and φ_{M_2} denote the tidal strain-velocity sensitivity and phase shift between the tidal strain and velocity variations for the M_2 tide, respectively. The covariance of the initial value was assumed to be equal to that of the prior model. Using the quasi-Newton method (Zhu et al., 1997), the logarithmic likelihood lnL was maximized with respect to the hyperparameters, searching for tidal strain responses from 0.001 to 1 % and phase shift from -180° to 180°, respectively. Considering a large covariance of the stretching parameter creates large short-term variations in seismic wave velocity, which could mask the negligible velocity variations induced by the tides. We set the search range of p_1 to account for long-term seasonal variations and short-term tidal responses. In particular, p_1 ranging from 2×10^{-13} to 5×10^{-10} varied the stretching parameters from 0.0001 % to 0.05 % linearly for three hours, whereas they were estimated up to 1 % for one month. Here we give an example of a station where the tidal response of velocity change is significant. The time series of the observed velocity variations without the explanatory variables at the N.SIKH station is presented in Figure 2 (a) and (b). The long-term variations in seismic wave velocity ranged from a few days to tens of days (Figure 2 (a)). Focusing on the velocity variations caused over a few days, the velocity variations can be observed with a half-day cycle (Figure 2 (b)). The power spectrum of the seismic wave velocity varied over two years and was estimated without the explanatory variables. In particular, they displayed a spectral peak corresponding to the semi-diurnal tidal variation (Figure 2 (c)). With the Maximum Likelihood method applied to determine the velocity variation related to the M_2 tide as an explanatory variable, the tidal response was estimated with statistical reliability. In Figure 2 (d), the spectral peak of the velocity variations during the period of M_2 tide disappeared because the velocity variation caused by M2 tide was extracted as the explanatory variable.

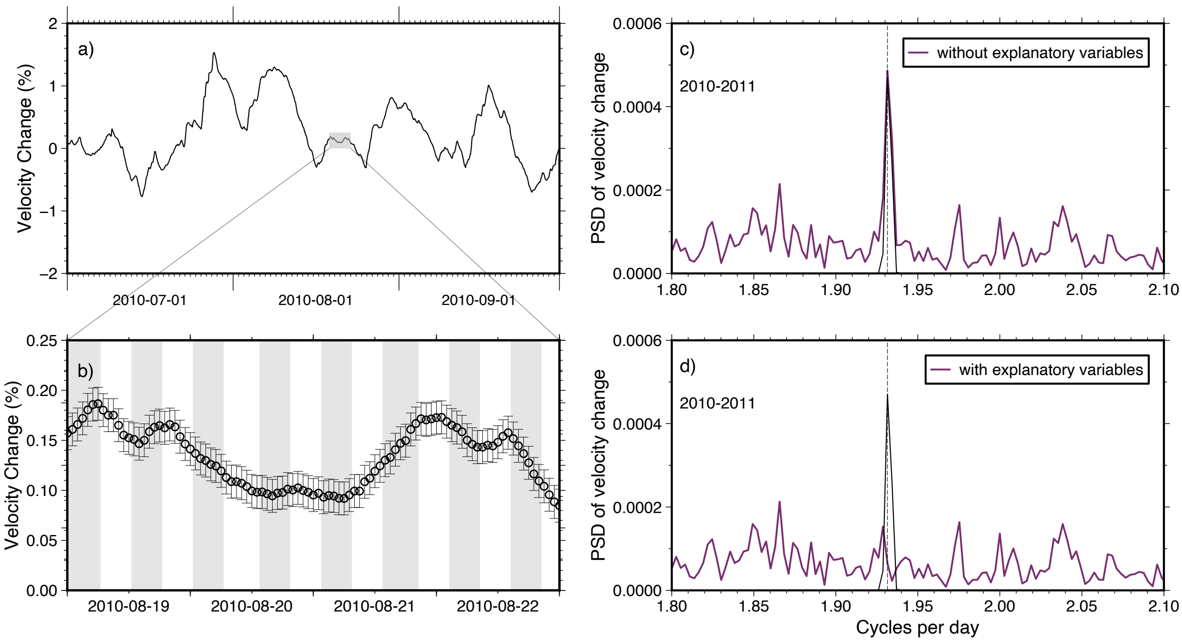

Figure 2. (a) Time series of velocity variations estimated without explanatory variables from 2010/7/1 to 2010/9/30 at N.SIKH station. (b) Enlarged view of the shaded region in Figure (a). The gray region depicts the period of contraction under M_2 tide. (c) The purple line denotes the power spectrum of velocity variations ($\%^2$/cycles per day). The black line displays the power spectrum of modeled velocity variations. Dashed-black line represents the cycles per day of the M_2 tide. The power spectrum was computed for the observed duration. (d) Power spectrum of velocity variations ($\%^2$/cycles per day) with the explanatory variables. The black line indicates the power spectrum of modeled velocity variations. Dashed-black line denotes the number of cycles per day of the M_2 tide.

To evaluate whether the observed velocity variations reliably respond to the tidal deformation, the appropriate number of hyperparameters was estimated using the AIC (Akaike, 1974) defined as

$$AIC_K = -2\ln \hat{L}_K + 2K \tag{5}$$

where K denotes the number of hyperparameters and $\ln \hat{L}_K$ represents the logarithmic likelihood for K hyperparameters. We compared the AIC between the hyperparameters, including the tidal response of the velocity variations. If the increment of AIC ($\Delta AIC \equiv$

$AIC_K - AIC_{K-2}$) was less than zero, the hyperparameters including M_2 tides were deemed as appropriate. Among all stations, 56.5 % of the stations displayed a reliable tidal response to the velocity variations.

4 Results

The spatial distribution of the velocity variations in response to M_2 tide and the phase delay of the seismic velocity variations with respect to the tidal strain is illustrated in Figure 3 (a) and (c), respectively, which were estimated as the hyperparameters using the Maximum Likelihood method. The stations with AIC increments less than 0 are displayed in the figure. The velocity variations in response to the M_2 tide were estimated up to 0.35 %. At stations with ΔAIC greater than 0, the velocity variations were generally estimated as less than 0.001 %, indicating that the tidal response to the velocity variations was not statistically significant (Figure S2). The phase delay of velocity changes with respect to the M_2 tide is expressed in the supplemental information (refer to Text S4).

Based on the velocity variations, dv/v, related to the M_2 tide and maximum volumetric strain of the M_2 tide, ε, on the ground surface computed by GOTIC2, we can infer the strain–velocity sensitivity, $\frac{dv/v}{\varepsilon}$, at each station. The spatial distribution of strain–velocity sensitivity is illustrated in Figure 3 (b). The strain–velocity sensitivities varied from approximately 10^3 to 10^5. The magnitude of the strain–velocity sensitivity was consistent with previous studies estimating the strain–velocity sensitivity in the shallow portion of the crust (Takano et al., 2014, 2019; Hillers et al., 2015; Sens-Schönfelder & Eulenfeld, 2019). Although the seismic velocity variations at each station were independently evaluated, the spatial distribution of the tidal response to the velocity variations displayed a characteristic spatial pattern. In addition, the spatial distributions of the tidal response to the velocity variations were compared with the geological setting of the Japanese islands. The locations of the active faults obtained from the digital map (Nakata & Imaizumi, 2002) and active volcanoes are presented in Figure 3 (d). First, a large tidal response was observed in the Kyushu region, where active volcanoes along the Ryukyu arc volcanic front and the median tectonic line were located. Certain stations in the Shikoku region, intersecting with the median tectonic line, exhibited a large tidal response to velocity variations. The regions spanning from central Japan to the Kinki region, where several active seismic faults have been detected, were characterized by large tidal responses. Although the southern portion of the Chubu region facing the Pacific Ocean exhibits a small

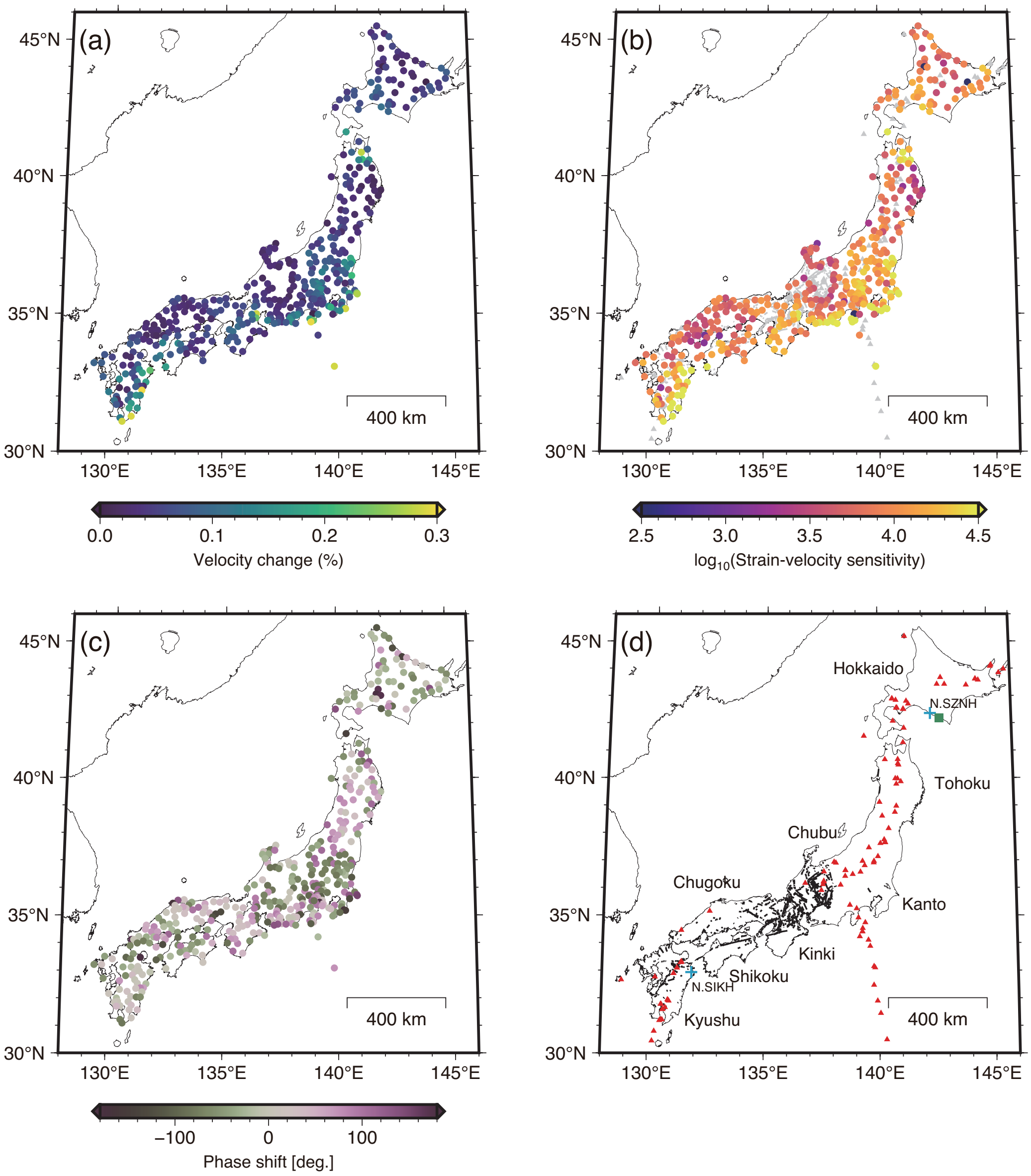

Figure 3. (a) Spatial distribution of velocity variations in response to the M_2 tide. (b) Spatial distribution of tidal strain response of velocity variations. Active volcanoes and faults are plotted in gray color. (c) Spatial distribution of phase delay of seismic velocity variations in response to tidal deformation. (d) Geological features in Japan. Red triangles display active volcanoes; solid-black lines represent active faults (Nakata & Imaizumi, 2002); the blue addition symbol indicates the location of N.SIKH station and N.SZNH station; the green square denotes the location of the tidal gauge. In (a), (b), and (c), the stations with AIC increments less than 0 are plotted.

tidal strain, it produced a larger tidal strain response compared to the surrounding area. In Kanto and the eastern portion of the Chubu region, a large tidal response to velocity variations was observed in the area east of the Niigata-Kobe Tectonic Line, wherein a high strain rate was observed to be dominated by a large contraction in the WNW—ESE direction (Sagiya et al., 2000). In the Tohoku region, the back-arc area of the Tohoku region generated a slightly larger tidal response than the island arc area of the region. In particular, the northern tip of the Tohoku region displayed a large tidal response. Moreover, a small tidal response to the velocity variations was observed in the central region of Hokkaido. However, the tidal response to the velocity variations was not strongly correlated with the geological features.

To systematically investigate the tidal response characteristics based on the velocity variations, we compared the strain–velocity sensitivity with the S-wave velocity structure estimated from the cross-correlations of microseisms using Hi-net seismic stations (Nishida et al., 2008). According to the depth sensitivity of the ambient noise correlations observed in this study, we compared the strain–velocity sensitivity with the S-wave velocity from the elevation at which the sensor was deployed to a depth of 1 km. The strain–velocity sensitivity against the S-wave velocity at each seismic station is presented in Figure 4, wherein the mean of 100 bootstrap-resamplings of strain-velocity sensitivity was plotted with a standard deviation of 0.06 km/s for bins with 50 % overlapping in S-wave velocity. For each bin, the average strain–velocity sensitivity increased linearly as the S-wave velocity decreased. However, the tidal strain response to the velocity varied considerably. Although the variations in the tidal response at the same S-wave velocity may be caused by various geomaterials, the statistical trend of the tidal response suggested certain common physical characteristics. Notably, the tomographic model of S-wave velocity and the autocorrelation function in this study has different spatial resolution. At certain stations, the region in which the autocorrelation function propagated does not necessarily correspond to the S-wave velocity structure estimated by cross-correlation functions of ambient noise, which may alter the relationship between the strain and velocity sensitivity and S-wave velocity.

5 Discussion

We extracted the tidal responses of the seismic velocity variations based on a state-space model. The tidal responses to the seismic velocity variations exhibited a charac-

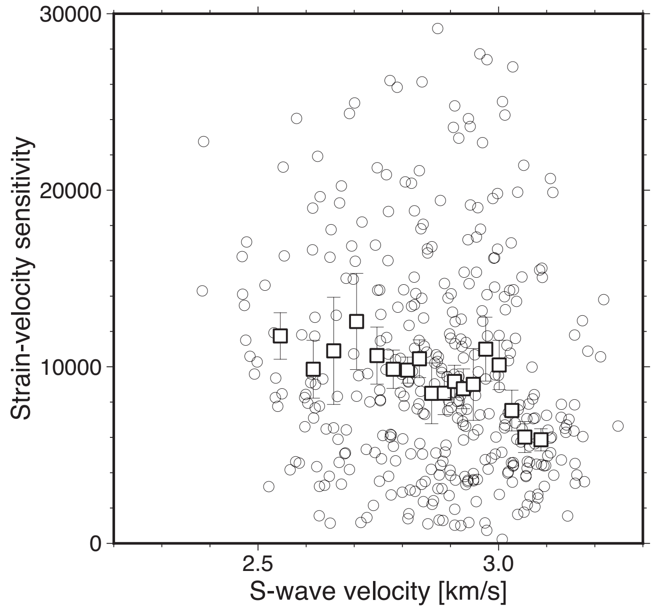

Figure 4. Relationship between S-wave velocity at depth of 1 km, and strain–velocity sensitivity at each station. White circles depict strain–velocity sensitivity at each station, and squares portray the mean of 100 bootstrap-resamplings of strain–velocity sensitivity for bins of 0.06 km/s in S-wave velocity.

teristic spatial pattern. In particular, the tidal strain response of velocity variations tended to increase in the low S-wave velocity regions in the shallow crust. The mechanism through which the seismic velocities respond to deformations is commonly interpreted as the opening and closing of microcracks in a medium (Walsh, 1965). If the rock strain indicates a nonhysteresis function of the confining pressure P_c and pore pressure P_o, the strain sensitivity of the velocity variations in the grain material can be formulated assuming a small aspect ratio, such as follows Shapiro (2003):

$$\frac{1}{V_{S_0}}\frac{\partial V_S}{\partial \varepsilon} \sim \frac{1}{2\gamma^2}\phi_{c_0}\exp\left(-\frac{1}{\gamma}CP\right) \tag{6}$$

where γ represents the aspect ratio of the pore, V_{S_0} denotes the S-wave velocity in a static state, ϕ_{c_0} represents the porosity of intergranular pore defined as compliant porosity, C indicates the drained compressibility, and P represents the effective pressure. The effective pressure is defined in terms of the pore pressure P_o and confining pressure P_c as follows:

$$P = P_c - P_o. \tag{7}$$

As related in Equation 6, the strain sensitivity decreases with the increasing effective pressure. The aspect ratio of the pores or cracks also contributes to the sensitivity based on the squared values. According to Equation 6, the aspect ratio of pores along with the pore pressure and porosity of the intergranular pores contribute to the strain–velocity sensitivity. Thus, a detailed comparison of the strain–velocity sensitivities with the velocity structure of the crust is required to investigate the extent to which each factor contributes to the observed strain–velocity sensitivities. V_P/V_S in the rocks is sensitive to liquid compressibility, pore geometry, and liquid volume fraction. In contrast, the ratio of the fractional variations in V_S and V_P is sensitive to liquid compressibility and pore geometry (Takei, 2002). Upon comparing the present findings with V_P/V_S and the ratio of the fractional variations in V_S and V_P, we can employ the constraints on these crustal parameters.

Brenguier et al. (2014) estimated the seismic velocity susceptibility to the dynamic stress induced by the 2011 Tohoku-Oki earthquake. They interpreted the spatial distributions of the susceptibilities of seismic velocity based on the highly pressurized fluid situated beneath the active volcanoes in eastern Japan. However, the tidal strain response of the velocity variations surrounding the volcanic front in eastern Japan was not large. According to the surface wave wavelength in the frequency band of 0.2–0.5 Hz or the sensitivity kernel of diffused ballistic waves, the wavefield of autocorrelations is sensitive between the surface and a depth of a few kilometers, which is shallower than the depth sensitivity reported by Brenguier et al. (2014). The S-wave velocity structure inferred from the cross-correlations of microseisms (Nishida et al., 2008) situated 1 km beneath the volcanic front is not low in comparison with that of other regions because the spatial resolution of the correlations does not delineate the small-scale velocity perturbation of the magma chamber (Nagaoka et al., 2012). As the Hi-net stations are sparsely located in volcanic regions, autocorrelation analysis would create a small sample of information beneath the volcanoes. The lack of a sample of the tidal response of the velocity variations beneath the volcano may create a difference from the stress susceptibility of the velocity variations. Although the stress susceptibility illustrates high-pressure fluid movement activated by the Tohoku-Oki earthquake, the tidal response of the velocity variations exhibits the response of the crust to static strain during its quiescent state. Brenguier et al. (2014) assessed the transient response of the crust to the earthquake, whereas the current results demonstrated the crustal response to the semi-diurnal deformation. The variations between the spatial features of strain–velocity sensitivity and stress susceptibility (Brenguier et al., 2014) suggest various response behaviors of the crust. In the future, researchers need to consider both the transient and static responses of the crust to more comprehensively understand the mechanical properties of the crust in response to strain or stress.

6 Conclusions

In this study, we examined the seismic velocity variations in response to tides throughout Japan. Utilizing the dense seismic network in Japan, we investigated the spatial extent of the tidal strain–velocity sensitivities. Accordingly, we extracted the tidal responses to velocity variations from the hourly stacked noise autocorrelations by combining the extended Kalman filter with the Maximum Likelihood method. The strain–velocity sensitivities varied from approximately 10^3 to 10^5. Upon comparing the strain–velocity sensitivity with the S-wave velocity structure in Japan, the tidal response to seismic velocity variations was larger at low S-wave velocities in the shallow crust. Based on the strain–velocity relationship in the grain material, the current results implied that the spatial variations in the tidal response of seismic wave velocity can potentially characterize the fluid pressure or shape of pores in the crust. The tidal responses to velocity variations in various time periods were extracted to investigate the temporal variations in the mechanical properties of the shallow crust. Future studies can utilize dense seismic networks such as a Large N-array or DAS observation to attain a higher spatial resolution of tidal strain–velocity sensitivity.

Open Research

We used data from Hi-net (doi.org/10.17598/nied.0003) managed by the National Research Institute for Earth Science and Disaster Prevention (NIED), Japan. The python code of the extended Kalman filter is also available on the Zenodo web page (https://zenodo.org/record/7476091#.Y8_BluzP20p).

Acknowledgments

The authors are grateful to people for maintaining the network and making the data readily available. This work was supported by JSPS KAKENHI Grand Number JP22K14110.

This work made use of ObsPy (Beyreuther et al., 2010), Numpy (Van Der Walt et al., 2011) and SciPy (Virtanen et al., 2020), and GMT programs (Wessel & Smith, 1998).

References

Akaike, H. (1974). A new look at the statistical model identification. *IEEE transactions on automatic control*, *19*(6), 716–723.

Beyreuther, M., Barsch, R., Krischer, L., Megies, T., Behr, Y., & Wassermann, J. (2010). Obspy: A python toolbox for seismology. *Seismological Research Letters*, *81*(3), 530–533.

Brenguier, F., Campillo, M., Hadziioannou, C., Shapiro, N. M., Nadeau, R. M., & Larose, E. (2008). Postseismic relaxation along the san andreas fault at parkfield from continuous seismological observations. *science*, *321*(5895), 1478–1481.

Brenguier, F., Campillo, M., Takeda, T., Aoki, Y., Shapiro, N., Briand, X., . . . Miyake, H. (2014). Mapping pressurized volcanic fluids from induced crustal seismic velocity drops. *Science*, *345*(6192), 80–82.

Brenguier, F., Shapiro, N. M., Campillo, M., Ferrazzini, V., Duputel, Z., Coutant, O., & Nercessian, A. (2008). Towards forecasting volcanic eruptions using seismic noise. *Nature Geoscience*, *1*(2), 126–130.

Cartwright, D., & Edden, A. C. (1973). Corrected tables of tidal harmonics. *Geophysical journal international*, *33*(3), 253–264.

De Fazio, T. L., Aki, K., & Alba, J. (1973). Solid earth tide and observed change in the in situ seismic velocity. *Journal of Geophysical Research*, *78*(8), 1319–1322.

Durbin, J., & Koopman, S. J. (2012). *Time series analysis by state space methods* (Vol. 38). OUP Oxford.

Hillers, G., Retailleau, L., Campillo, M., Inbal, A., Ampuero, J.-P., & Nishimura, T. (2015). In situ observations of velocity changes in response to tidal deformation from analysis of the high-frequency ambient wavefield. *Journal of Geophysical Research: Solid Earth*, *120*(1), 210–225.

Hobiger, M., Wegler, U., Shiomi, K., & Nakahara, H. (2014). Single-station cross-correlation analysis of ambient seismic noise: application to stations in the surroundings of the 2008 iwate-miyagi nairiku earthquake. *Geophysical Journal*

International, *198*(1), 90–109.

Maeda, T., Obara, K., Furumura, T., & Saito, T. (2011). Interference of long-period seismic wavefield observed by the dense hi-net array in japan. *Journal of Geophysical Research: Solid Earth*, *116*(B10).

Mao, S., Campillo, M., van der Hilst, R. D., Brenguier, F., Stehly, L., & Hillers, G. (2019). High temporal resolution monitoring of small variations in crustal strain by dense seismic arrays. *Geophysical Research Letters*, *46*(1), 128–137.

Matsumoto, K., Sato, T., Takanezawa, T., & Ooe, M. (2001). Gotic2: A program for computation of oceanic tidal loading effect. *Journal of the Geodetic Society of Japan*, *47*(1), 243–248.

Nagaoka, Y., Nishida, K., Aoki, Y., Takeo, M., & Ohminato, T. (2012). Seismic imaging of magma chamber beneath an active volcano. *Earth and Planetary Science Letters*, *333*, 1–8.

Nakata, T., & Imaizumi, T. (2002). *Digital active fault map of japan.* University of Tokyo Press, Tokyo.

Nishida, K., Kawakatsu, H., & Obara, K. (2008). Three-dimensional crustal s wave velocity structure in japan using microseismic data recorded by hi-net tiltmeters. *Journal of Geophysical Research: Solid Earth*, *113*(B10).

Nishida, K., Mizutani, Y., Ichihara, M., & Aoki, Y. (2020). Time-lapse monitoring of seismic velocity associated with 2011 shinmoe-dake eruption using seismic interferometry: An extended kalman filter approach. *Journal of Geophysical Research: Solid Earth*, *125*(9), e2020JB020180.

Obermann, A., & Hillers, G. (2019). Seismic time-lapse interferometry across scales. In *Advances in geophysics* (Vol. 60, pp. 65–143). Elsevier.

Reasenberg, P., & Aki, K. (1974). A precise, continuous measurement of seismic velocity for monitoring in situ stress. *Journal of Geophysical Research*, *79*(2), 399–406.

Sagiya, T., Miyazaki, S., & Tada, T. (2000). Continuous gps array and present-day crustal deformation of japan. *Pure and applied Geophysics*, *157*(11), 2303–2322.

Sens-Schönfelder, C., & Eulenfeld, T. (2019). Probing the in situ elastic nonlinearity of rocks with earth tides and seismic noise. *Physical review letters*, *122*(13), 138501.

Shapiro, S. A. (2003). Elastic piezosensitivity of porous and fractured rocks. *Geophysics*, *68*(2), 482–486.

Takagi, R., Nishida, K., Aoki, Y., Maeda, T., Masuda, K., Takeo, M., … Saito, K. (2015). A single bit matters: Coherent noise of seismic data loggers. *Seismological Research Letters*, *86*(3), 901–907.

Takano, T., Nishimura, T., & Nakahara, H. (2017). Seismic velocity changes concentrated at the shallow structure as inferred from correlation analyses of ambient noise during volcano deformation at izu-oshima, japan. *Journal of Geophysical Research: Solid Earth*, *122*(8), 6721–6736.

Takano, T., Nishimura, T., Nakahara, H., Ohta, Y., & Tanaka, S. (2014). Seismic velocity changes caused by the earth tide: Ambient noise correlation analyses of small-array data. *Geophysical Research Letters*, *41*(17), 6131–6136.

Takano, T., Nishimura, T., Nakahara, H., Ueda, H., & Fujita, E. (2019). Sensitivity of seismic velocity changes to the tidal strain at different lapse times: Data analyses of a small seismic array at izu-oshima volcano. *Journal of Geophysical Research: Solid Earth*, *124*(3), 3011–3023.

Takei, Y. (2002). Effect of pore geometry on vp/vs: From equilibrium geometry to crack. *Journal of Geophysical Research: Solid Earth*, *107*(B2), ECV–6.

Van Der Walt, S., Colbert, S. C., & Varoquaux, G. (2011). The numpy array: a structure for efficient numerical computation. *Computing in science & engineering*, *13*(2), 22–30.

Virtanen, P., Gommers, R., Oliphant, T. E., Haberland, M., Reddy, T., Cournapeau, D., … others (2020). Scipy 1.0: fundamental algorithms for scientific computing in python. *Nature methods*, *17*(3), 261–272.

Walsh, J. (1965). The effect of cracks on the uniaxial elastic compression of rocks. *Journal of Geophysical Research*, *70*(2), 399–411.

Weaver, R. L., & Lobkis, O. I. (2000). Temperature dependence of diffuse field phase. *Ultrasonics*, *38*(1-8), 491–494.

Wessel, P., & Smith, W. H. (1998). New, improved version of generic mapping tools released. *Eos, Transactions American Geophysical Union*, *79*(47), 579–579.

Yamamura, K., Sano, O., Utada, H., Takei, Y., Nakao, S., & Fukao, Y. (2003). Long-term observation of in situ seismic velocity and attenuation. *Journal of Geophysical Research: Solid Earth*, *108*(B6).

Zhu, C., Byrd, R. H., Lu, P., & Nocedal, J. (1997). Algorithm 778: L-bfgs-b: Fortran subroutines for large-scale bound-constrained optimization. *ACM Transactions on mathematical software (TOMS)*, *23*(4), 550–560.

Tidal response of seismic wave velocity at shallow crust in Japan

Tomoya Takano[1] and Kiwamu Nishida[2]

[1]Graduate School of Science and Technology, Hirosaki University
[2]Earthquake Research Institute, the University of Tokyo

Key Points:

- The spatial distribution of seismic velocity changes caused by tides was determined using dense network of seismic stations in Japan.
- The tidal response to velocity changes was extracted from ambient noise using an extended Kalman filter with a Maximum Likelihood method.
- Strain–velocity sensitivities tend to increase at a low S-wave velocity in the shallow crust.

Corresponding author: Tomoya Takano, `takanot@hirosaki-u.ac.jp`

Abstract

Microcracks in geomaterials cause variations in the elastic moduli under applied strain, thereby creating seismic wave velocity variations. These are crucial for understanding the dynamic processes of the crust, such as fault-zone damage, healing, and volcanic activities. Solid earth tides have been used to detect seismic velocity changes responding to crustal-scale deformations. However, no prior research has explored the characteristics of the seismic velocity variations caused by large-scale tidal deformation. To systematically evaluate the tidal response to velocity variations, we developed a new method that utilized the flexibility of a state-space model. The tidal response was derived from hourly stacked noise autocorrelations using a seismic interferometry method throughout Japan. In particular, large tide-induced seismic velocities were observed in the low S-wave velocity region of the shallow crust. Overall, the tidal responses to velocity variations can provide new insights into the response mechanisms of the shallow crust to applied strain.

Plain Language Summary

Rock deformations can open or close microcracks in rocks along with varying their elastic moduli under an applied strain. The temporal variations in the elastic moduli of rocks alter the seismic wave velocity, which can be monitored to provide information on the strain applied to the crust. This is crucial for understanding the geological processes in the fault zones and volcanic regions. To utilize the seismic velocity variations for monitoring how much the Earth's structure deforms, the response of the seismic velocity to the deformations must be assessed. The deformation of the Earth's surface caused by the gravity of the Moon and Sun, which is called solid Earth tides, has been used to study seismic velocity variations in response to crustal deformation. However, only a limited number of regions have been studied for the tidal response of the seismic velocity, and the characteristics of its variations caused by tidal deformation were not yet apparent. This study measured the tidal responses to seismic velocity variations throughout Japan with reliable estimations. Notably, the tide-induced seismic velocity variations tend to increase in the low S-wave velocity region. Overall, these results provide new insights into the response mechanisms of the shallow crust to deformations.

1 Introduction

The temporal evolution of the stress or strain applied to the crust provides essential information for understanding the dynamic processes in fault zones and active volcanoes. This is because the occurrence of earthquakes depends on the stress or strain state of the Earth and the fluid distribution around the fault. Volcanic eruptions occur because of the pressure accumulation under volcanic fluid pressurization and magma supply from deeper regions. Upon observing the response of the crust to the applied stress or strain, the in-situ stress or strain variations in the crust can be estimated, which generally involve limitations in the case of direct measurement. The geomaterials in the crust are nonlinearly elastic (Walsh, 1965), and their elastic moduli vary with the applied strain. As the seismic wave velocity depends on the elastic moduli, the applied strain induces variations in the seismic wave velocity. Therefore, tracking the seismic wave velocity variations can adequately serve as a proxy for examining the temporal variations in the elastic constants caused by the applied strain in the crust. Previous studies have reported that the temporal variations in the seismic wave velocity are associated with the static strain variations induced by, for instance, large earthquakes (e.g. Brenguier, Campillo, et al., 2008) and volcanic activities (e.g. Brenguier, Shapiro, et al., 2008; Takano et al., 2017). To monitor the applied strain in the crust and its responses, the variations in the seismic wave velocity response to a given strain perturbation must be examined.

As we can precisely compute the static strain caused by a solid earth tide, the seismic velocity variations associated with the tidal strain provide information on the strain–velocity relationships on Earth. Earlier, in controlled active seismic experiments, the seismic velocity observably varied with the tidal strain (e.g. De Fazio et al., 1973; Reasenberg & Aki, 1974; Yamamura et al., 2003). However, active seismic experiments do not yield temporal resolution and constrained locations in repeated experiments. Recently, a passive noise-based technique (e.g. Obermann & Hillers, 2019) observed seismic velocity variations related to tides (e.g. Takano et al., 2014, 2019; Sens-Schönfelder & Eulenfeld, 2019; Hillers et al., 2015; Mao et al., 2019). To estimate the velocity variations caused by tides, two strategies have been employed using ambient noise correlations. The first one involves the stacking of ambient noise correlations according to the tidal deformation amplitude and measuring the phase differences between the noise correlations during the dilatation and contraction of the crust (Takano et al., 2014; Hillers et al., 2015; Takano et al., 2019). After stacking the noise correlations for a long time period, the velocity variations caused by the nontidal effects can be canceled. The second one examines the velocity variations corresponding to the tidal harmonics from the spectrum of seismic velocity variations with high temporal sampling (Sens-Schönfelder & Eulenfeld, 2019). These previous studies estimated the strain–velocity sensitivities based on the velocity variations induced by tidal deformation at depths shallower than a few kilometers. As such, the estimated magnitudes of strain–velocity sensitivity may depend on the strength of nonlinear elasticity at their location. Previous studies have employed several methods to detect the tidal responses of velocity variations and the spatial sensitivities of wavefields. The tidal responses to velocity variations have been detected in certain regions. However, no existing research has reported the spatial features of the seismic velocity variations observed in response to crustal-scale deformation. In order to estimate the spatial distribution of velocity changes in response to tides, it is necessary to measure the response using a uniform method and establish criteria for determining whether the seismic wave velocity responds to tides. This study aims to calculate the tidal response of the velocity variations in the shallow crust throughout Japan for proposing the criteria for detecting these tidal responses.

To estimate the variations in only seismic velocity related to tidal strain, the tidal response to the velocity variations must be accurately separated from the other causes of seismic velocity variations. Recently, Nishida et al. (2020) developed a novel method for estimating the seismic velocity variations using an extended Kalman filter based on a state-space model (e.g. Durbin & Koopman, 2012). They utilized an extended Kalman filter algorithm to estimate the seismic velocity variations as a state variable and used the Maximum Likelihood method to estimate the hyperparameters describing the velocity variations related to precipitation and large earthquakes. The flexibility of the state-space model for the time-series data can easily incorporate the seismic wave velocity variations induced by external perturbations into the model. As the period, phase, and amplitude of the tides were accurately determined in advance, the superposition of the periodic functions can model the tide-induced velocity variations. Thus, the tidal responses to the velocity variations were incorporated into the state-space model as hyperparameters to systematically estimate the tidal strain response using the extended Kalman filter and Maximum Likelihood method.

In this study, we investigated the seismic velocity variations in response to tidal strains throughout Japan. First, the nine components of the ambient-noise autocorrelation functions were calculated using Japan's dense seismic network. Thereafter, we extracted the seismic velocity variations related to the tide from the hourly stacked-noise correlation functions using an extended Kalman filter with a Maximum Likelihood method. The observed strain–velocity sensitivities were compared with the S-wave velocity structure at each station. The spatial distribution of the tide-induced velocity variations was studied to characterize the mechanical properties of the shallow crust in response to deformation. As the tides and seismic ambient noise can be observed at any location and instant, the flexibility of the state-space model will enable us to attain a higher spatial resolution of the tidal strain–velocity sensitivities with a dense seismic network, such as a Large N-array or Distributed Acoustic Sensing (DAS) observation.

2 Data

To detect the tidal response of seismic wave velocity variations, we computed the autocorrelation functions of ambient noise at a single station using 796 Hi-net seismic stations operated by the National Research Institute for Earth Science and Disaster Prevention (NIED). As most of the Hi-net network stations include the same borehole-type sensors, the characteristics among instruments will vary less. The location map of the seismic stations with the maximum tidal volumetric strain at the ground surface computed by GOTIC2 (Matsumoto et al., 2001) is illustrated in Figure 1. GOTIC2 computes the tidal strain, including the solid earth tide and ocean load. In the GOTIC2 program, ocean loading was computed with a five-minute resolution around Japan. The NIED deployed three-component velocity meters with a natural frequency of 1 Hz at the bottom of each borehole located at a depth of about 100 m or more at most stations. After subtracting the common data logger noise (Takagi et al., 2015), the instrumental responses of the seismometers were deconvolved using the inverse filtering technique (Maeda et al., 2011). We resampled the data to 2 Hz to efficiently compute the correlation functions. For each station every hour, we computed three components (north–north, east–east, upward–upward) of an auto-correlation function and six components (east–north, east–upward, north–east, north–upward, upward–east, and upward–north) of a single-station cross-correlation (Hobiger et al., 2014). The correlation functions were filtered at frequency bands of 0.2–0.5 Hz. In summary, we analyzed the ambient noise recorded from January 1, 2010, to December 31, 2011.

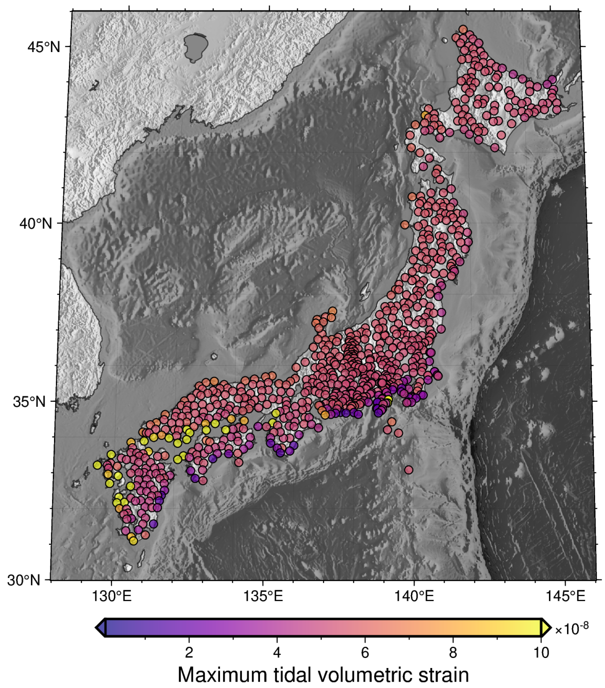

Figure 1. Location map of seismic stations. The color scale displays the maximum volumetric tidal strain during the observation period.

3 Method

The tidal response of seismic velocity variations was determined from the hourly stacked noise correlations using the extended Kalman filter with the Maximum Likelihood method based on the state-space model (Nishida et al., 2020). In Kalman filter processing, we minimized the squared differences between the model correlation function predicted from one previous step and the observed correlations. Assuming that the temporal variations of the seismic wave velocity in a given medium occur homogeneously, a model function of the observed correlations can be expressed by altering the amplitude and stretching factor of the reference correlation function using a stretching method in the time domain (Weaver & Lobkis, 2000). The stretching method has been linearized for application to a Kalman filter (Nishida et al., 2020). The tidal response of the velocity variations was determined as the explanatory variables in a state-space model in two steps. First, the temporal variations of amplitude and the stretching factor of the correlations were estimated as state variables in a state-space model with Kalman Filter processing. Second, the tidal response to the velocity variations was determined as an explanatory variable, referred to as a hyperparameter, using the Maximum Likelihood method. Thus, we constructed a state-space model as follows:

$$\boldsymbol{y}_t^p = \boldsymbol{m}^p \left(\boldsymbol{\alpha}_t + \boldsymbol{R}_t\right) + \boldsymbol{\epsilon}_t, \qquad \boldsymbol{\epsilon}_t \sim \mathcal{N}\left(0, \boldsymbol{H}_t\right) \tag{1}$$

$$\boldsymbol{\alpha}_{t+1} = \boldsymbol{\alpha}_t + \boldsymbol{\eta}_t, \qquad \boldsymbol{\eta}_t \sim \mathcal{N}\left(0, \boldsymbol{Q}_t\right), \tag{2}$$

where $\boldsymbol{y}_t^p$ denotes the data vector of the observed correlations for the p th component, $\boldsymbol{\alpha}_t$ represents the state vector, $\boldsymbol{R}_t$ symbolizes the explanatory variable related to the tides, and $\boldsymbol{\epsilon}_t$ and $\boldsymbol{\eta}_t$ indicate the mutually independent random variables subject to a normal distribution ($\mathcal{N}$) with zero means and covariance matrix $\boldsymbol{H_t}$ and $\boldsymbol{Q_t}$, respectively. The equations 1 and 2 have been elaborately expressed in the supplemental information (refer to Text S1).

To compute the reference correlation at each station, we first estimated the state variables of the stretching factor and amplitude common across all nine components without any explanatory variables. Thereafter, the reference correlation was estimated by averaging the observed correlations stretched with the estimated amplitude and stretching factor for the observation duration. Prior data covariance, h_0, was estimated based on the time average of the squared differences between the observed and reference correlations. The validation of prior data covariance is described in the supplemental information (Text S2). The state variables were estimated through the recursive linear Kalman filter and smoother (Durbin & Koopman, 2012) by adjusting the explanatory variables, initial stretching factor, and prior model covariance for the initial value.

The tidal response of the seismic wave velocity was modeled by adding the cosine functions related to the tidal constituents as follows:

$$r_t = \sum_{m=1}^{M} A_m \cos\left(\omega_m t + \varphi_m + \theta_m\right) \tag{3}$$

where m denotes the index of the tidal constituents, A_m indicates the sensitivity of the seismic wave velocity to tidal strain, φ_m represents the phase angle of the tide, ω_m denotes the angular frequency of the tide, and θ_m represents the difference between the tidal strain and the observed variations in seismic velocity. A phase delay may occur in the response of the velocity variations to tidal strain caused by the nonlinear elasticity of the rock (Sens-Schönfelder & Eulenfeld, 2019). φ_m was estimated from the theoretical tidal strain computed using GOTIC2 at each station, whereas ω_m was obtained from the table of tidal constituents (Cartwright & Edden, 1973). The velocity variations related to only M_2 tide were incorporated into the modeled tidal response of the seismic wave velocity, which most significantly contributed to the seismic wave velocity variations in the tidal constituents (Sens-Schönfelder & Eulenfeld, 2019). As the M_2 tide originated from the moon, the thermoelastic effects did not contribute to the seismic velocity variations.

The logarithmic likelihood $\ln L$ was maximized with respect to the hyperparameters. $\ln L$ was computed following the Kalman filtering processes (e.g. Durbin & Koopman, 2012); $\ln L$ is a function of hyperparameter β as

$$\beta = (p_0, p_1, \gamma_1, A_{M_2}, \varphi_{M_2})\,, \tag{4}$$

where p_0 and p_1 represent the covariance of the initial value of the amplitude and stretching factor, respectively, γ_1 denotes the initial value of the stretching factor, and A_{M_2} and φ_{M_2} denote the tidal strain-velocity sensitivity and phase shift between the tidal strain and velocity variations for the M_2 tide, respectively. The covariance of the initial value was assumed to be equal to that of the prior model. Using the quasi-Newton method (Zhu et al., 1997), the logarithmic likelihood lnL was maximized with respect to the hyperparameters, searching for tidal strain responses from 0.001 to 1 % and phase shift from -180° to 180°, respectively. Considering a large covariance of the stretching parameter creates large short-term variations in seismic wave velocity, which could mask the negligible velocity variations induced by the tides. We set the search range of p_1 to account for long-term seasonal variations and short-term tidal responses. In particular, p_1 ranging from 2×10^{-13} to 5×10^{-10} varied the stretching parameters from 0.0001 % to 0.05 % linearly for three hours, whereas they were estimated up to 1 % for one month. Here we give an example of a station where the tidal response of velocity change is significant. The time series of the observed velocity variations without the explanatory variables at the N.SIKH station is presented in Figure 2 (a) and (b). The long-term variations in seismic wave velocity ranged from a few days to tens of days (Figure 2 (a)). Focusing on the velocity variations caused over a few days, the velocity variations can be observed with a half-day cycle (Figure 2 (b)). The power spectrum of the seismic wave velocity varied over two years and was estimated without the explanatory variables. In particular, they displayed a spectral peak corresponding to the semi-diurnal tidal variation (Figure 2 (c)). With the Maximum Likelihood method applied to determine the velocity variation related to the M_2 tide as an explanatory variable, the tidal response was estimated with statistical reliability. In Figure 2 (d), the spectral peak of the velocity variations during the period of M_2 tide disappeared because the velocity variation caused by M2 tide was extracted as the explanatory variable.

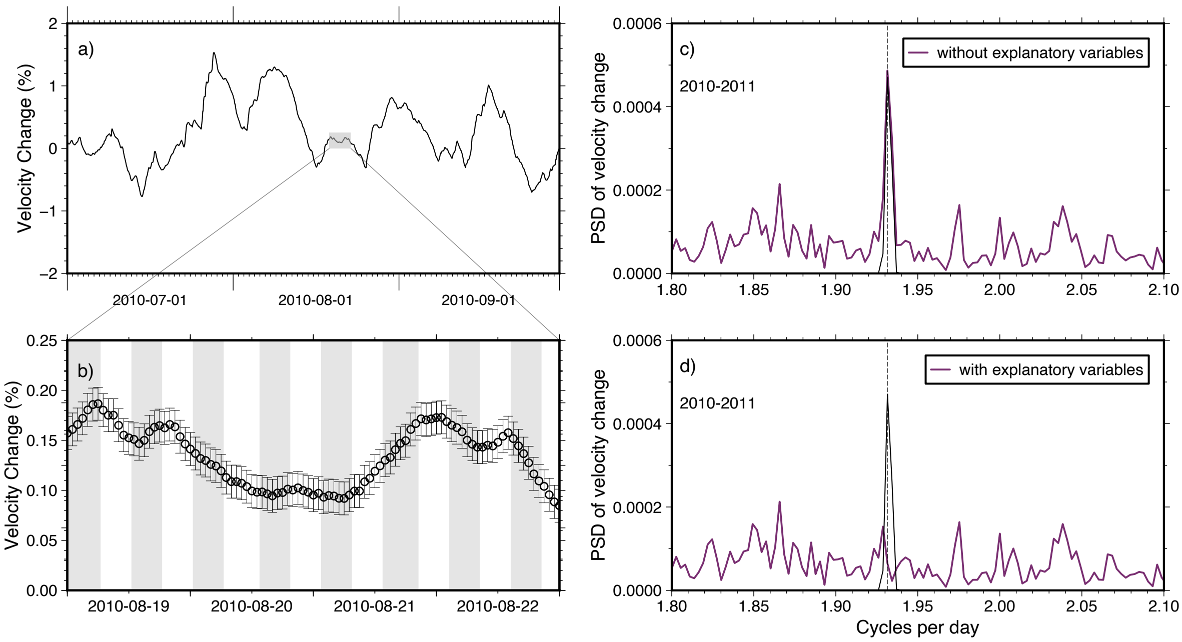

Figure 2. (a) Time series of velocity variations estimated without explanatory variables from 2010/7/1 to 2010/9/30 at N.SIKH station. (b) Enlarged view of the shaded region in Figure (a). The gray region depicts the period of contraction under M_2 tide. (c) The purple line denotes the power spectrum of velocity variations ($\%^2$/cycles per day). The black line displays the power spectrum of modeled velocity variations. Dashed-black line represents the cycles per day of the M_2 tide. The power spectrum was computed for the observed duration. (d) Power spectrum of velocity variations ($\%^2$/cycles per day) with the explanatory variables. The black line indicates the power spectrum of modeled velocity variations. Dashed-black line denotes the number of cycles per day of the M_2 tide.

To evaluate whether the observed velocity variations reliably respond to the tidal deformation, the appropriate number of hyperparameters was estimated using the AIC (Akaike, 1974) defined as

$$AIC_K = -2 \ln \hat{L}_K + 2K \tag{5}$$

where K denotes the number of hyperparameters and $\ln \hat{L}_K$ represents the logarithmic likelihood for K hyperparameters. We compared the AIC between the hyperparameters, including the tidal response of the velocity variations. If the increment of AIC ($\Delta AIC \equiv$

$AIC_K - AIC_{K-2}$) was less than zero, the hyperparameters including M_2 tides were deemed as appropriate. Among all stations, 56.5 % of the stations displayed a reliable tidal response to the velocity variations.

4 Results

The spatial distribution of the velocity variations in response to M_2 tide and the phase delay of the seismic velocity variations with respect to the tidal strain is illustrated in Figure 3 (a) and (c), respectively, which were estimated as the hyperparameters using the Maximum Likelihood method. The stations with AIC increments less than 0 are displayed in the figure. The velocity variations in response to the M_2 tide were estimated up to 0.35 %. At stations with ΔAIC greater than 0, the velocity variations were generally estimated as less than 0.001 %, indicating that the tidal response to the velocity variations was not statistically significant (Figure S2). The phase delay of velocity changes with respect to the M_2 tide is expressed in the supplemental information (refer to Text S4).

Based on the velocity variations, dv/v, related to the M_2 tide and maximum volumetric strain of the M_2 tide, ε, on the ground surface computed by GOTIC2, we can infer the strain–velocity sensitivity, $\frac{dv/v}{\varepsilon}$, at each station. The spatial distribution of strain–velocity sensitivity is illustrated in Figure 3 (b). The strain–velocity sensitivities varied from approximately 10^3 to 10^5. The magnitude of the strain–velocity sensitivity was consistent with previous studies estimating the strain–velocity sensitivity in the shallow portion of the crust (Takano et al., 2014, 2019; Hillers et al., 2015; Sens-Schönfelder & Eulenfeld, 2019). Although the seismic velocity variations at each station were independently evaluated, the spatial distribution of the tidal response to the velocity variations displayed a characteristic spatial pattern. In addition, the spatial distributions of the tidal response to the velocity variations were compared with the geological setting of the Japanese islands. The locations of the active faults obtained from the digital map (Nakata & Imaizumi, 2002) and active volcanoes are presented in Figure 3 (d). First, a large tidal response was observed in the Kyushu region, where active volcanoes along the Ryukyu arc volcanic front and the median tectonic line were located. Certain stations in the Shikoku region, intersecting with the median tectonic line, exhibited a large tidal response to velocity variations. The regions spanning from central Japan to the Kinki region, where several active seismic faults have been detected, were characterized by large tidal responses. Although the southern portion of the Chubu region facing the Pacific Ocean exhibits a small

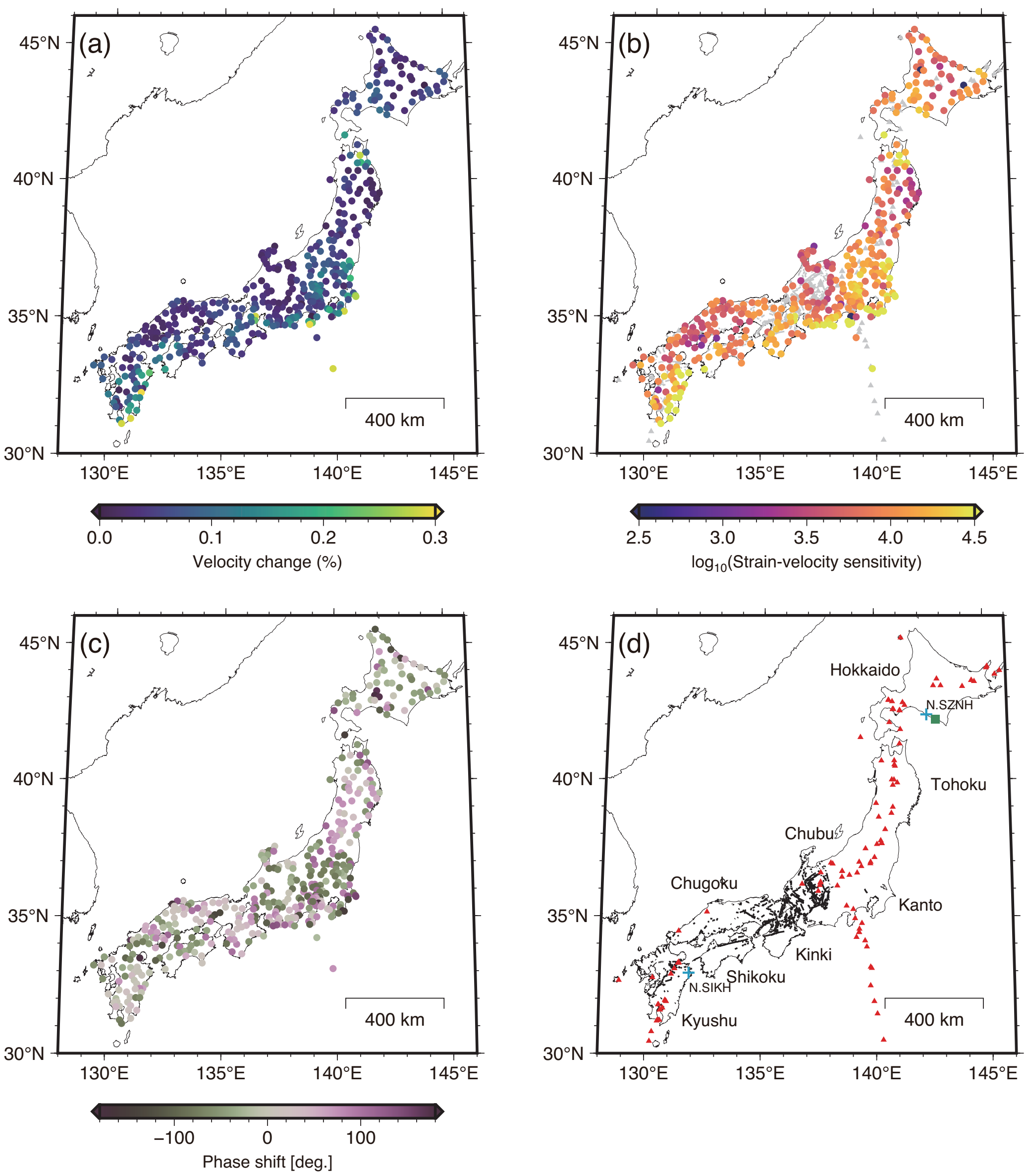

Figure 3. (a) Spatial distribution of velocity variations in response to the M_2 tide. (b) Spatial distribution of tidal strain response of velocity variations. Active volcanoes and faults are plotted in gray color. (c) Spatial distribution of phase delay of seismic velocity variations in response to tidal deformation. (d) Geological features in Japan. Red triangles display active volcanoes; solid-black lines represent active faults (Nakata & Imaizumi, 2002); the blue addition symbol indicates the location of N.SIKH station and N.SZNH station; the green square denotes the location of the tidal gauge. In (a), (b), and (c), the stations with AIC increments less than 0 are plotted.

tidal strain, it produced a larger tidal strain response compared to the surrounding area. In Kanto and the eastern portion of the Chubu region, a large tidal response to velocity variations was observed in the area east of the Niigata-Kobe Tectonic Line, wherein a high strain rate was observed to be dominated by a large contraction in the WNW—ESE direction (Sagiya et al., 2000). In the Tohoku region, the back-arc area of the Tohoku region generated a slightly larger tidal response than the island arc area of the region. In particular, the northern tip of the Tohoku region displayed a large tidal response. Moreover, a small tidal response to the velocity variations was observed in the central region of Hokkaido. However, the tidal response to the velocity variations was not strongly correlated with the geological features.

To systematically investigate the tidal response characteristics based on the velocity variations, we compared the strain–velocity sensitivity with the S-wave velocity structure estimated from the cross-correlations of microseisms using Hi-net seismic stations (Nishida et al., 2008). According to the depth sensitivity of the ambient noise correlations observed in this study, we compared the strain–velocity sensitivity with the S-wave velocity from the elevation at which the sensor was deployed to a depth of 1 km. The strain–velocity sensitivity against the S-wave velocity at each seismic station is presented in Figure 4, wherein the mean of 100 bootstrap-resamplings of strain-velocity sensitivity was plotted with a standard deviation of 0.06 km/s for bins with 50 % overlapping in S-wave velocity. For each bin, the average strain–velocity sensitivity increased linearly as the S-wave velocity decreased. However, the tidal strain response to the velocity varied considerably. Although the variations in the tidal response at the same S-wave velocity may be caused by various geomaterials, the statistical trend of the tidal response suggested certain common physical characteristics. Notably, the tomographic model of S-wave velocity and the autocorrelation function in this study has different spatial resolution. At certain stations, the region in which the autocorrelation function propagated does not necessarily correspond to the S-wave velocity structure estimated by cross-correlation functions of ambient noise, which may alter the relationship between the strain and velocity sensitivity and S-wave velocity.

5 Discussion

We extracted the tidal responses of the seismic velocity variations based on a state-space model. The tidal responses to the seismic velocity variations exhibited a charac-

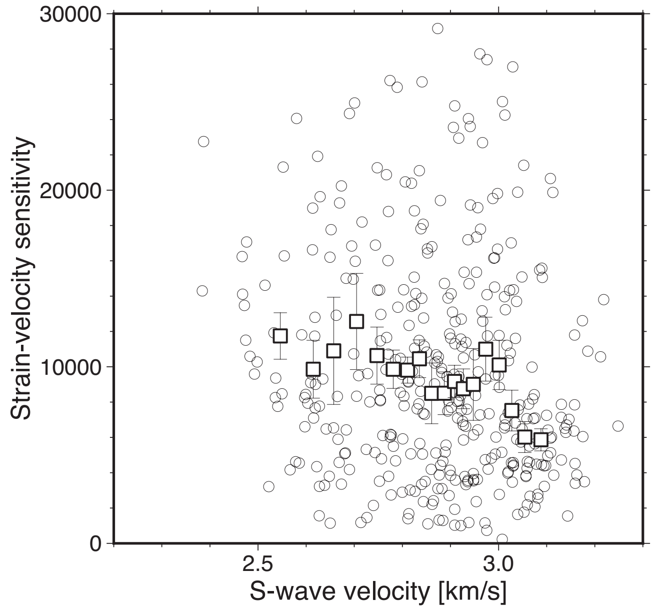

Figure 4. Relationship between S-wave velocity at depth of 1 km, and strain–velocity sensitivity at each station. White circles depict strain–velocity sensitivity at each station, and squares portray the mean of 100 bootstrap-resamplings of strain–velocity sensitivity for bins of 0.06 km/s in S-wave velocity.

teristic spatial pattern. In particular, the tidal strain response of velocity variations tended to increase in the low S-wave velocity regions in the shallow crust. The mechanism through which the seismic velocities respond to deformations is commonly interpreted as the opening and closing of microcracks in a medium (Walsh, 1965). If the rock strain indicates a nonhysteresis function of the confining pressure P_c and pore pressure P_o, the strain sensitivity of the velocity variations in the grain material can be formulated assuming a small aspect ratio, such as follows Shapiro (2003):

$$\frac{1}{V_{S_0}}\frac{\partial V_S}{\partial \varepsilon} \sim \frac{1}{2\gamma^2}\phi_{c_0}\exp\left(-\frac{1}{\gamma}CP\right) \tag{6}$$

where γ represents the aspect ratio of the pore, V_{S_0} denotes the S-wave velocity in a static state, ϕ_{c_0} represents the porosity of intergranular pore defined as compliant porosity, C indicates the drained compressibility, and P represents the effective pressure. The effective pressure is defined in terms of the pore pressure P_o and confining pressure P_c as follows:

$$P = P_c - P_o. \tag{7}$$

As related in Equation 6, the strain sensitivity decreases with the increasing effective pressure. The aspect ratio of the pores or cracks also contributes to the sensitivity based on the squared values. According to Equation 6, the aspect ratio of pores along with the pore pressure and porosity of the intergranular pores contribute to the strain–velocity sensitivity. Thus, a detailed comparison of the strain–velocity sensitivities with the velocity structure of the crust is required to investigate the extent to which each factor contributes to the observed strain–velocity sensitivities. V_P/V_S in the rocks is sensitive to liquid compressibility, pore geometry, and liquid volume fraction. In contrast, the ratio of the fractional variations in V_S and V_P is sensitive to liquid compressibility and pore geometry (Takei, 2002). Upon comparing the present findings with V_P/V_S and the ratio of the fractional variations in V_S and V_P, we can employ the constraints on these crustal parameters.

Brenguier et al. (2014) estimated the seismic velocity susceptibility to the dynamic stress induced by the 2011 Tohoku-Oki earthquake. They interpreted the spatial distributions of the susceptibilities of seismic velocity based on the highly pressurized fluid situated beneath the active volcanoes in eastern Japan. However, the tidal strain response of the velocity variations surrounding the volcanic front in eastern Japan was not large. According to the surface wave wavelength in the frequency band of 0.2–0.5 Hz or the sensitivity kernel of diffused ballistic waves, the wavefield of autocorrelations is sensitive between the surface and a depth of a few kilometers, which is shallower than the depth sensitivity reported by Brenguier et al. (2014). The S-wave velocity structure inferred from the cross-correlations of microseisms (Nishida et al., 2008) situated 1 km beneath the volcanic front is not low in comparison with that of other regions because the spatial resolution of the correlations does not delineate the small-scale velocity perturbation of the magma chamber (Nagaoka et al., 2012). As the Hi-net stations are sparsely located in volcanic regions, autocorrelation analysis would create a small sample of information beneath the volcanoes. The lack of a sample of the tidal response of the velocity variations beneath the volcano may create a difference from the stress susceptibility of the velocity variations. Although the stress susceptibility illustrates high-pressure fluid movement activated by the Tohoku-Oki earthquake, the tidal response of the velocity variations exhibits the response of the crust to static strain during its quiescent state. Brenguier et al. (2014) assessed the transient response of the crust to the earthquake, whereas the current results demonstrated the crustal response to the semi-diurnal deformation. The variations between the spatial features of strain–velocity sensitivity and stress susceptibility (Brenguier et al., 2014) suggest various response behaviors of the crust. In the future, researchers need to consider both the transient and static responses of the crust to more comprehensively understand the mechanical properties of the crust in response to strain or stress.

6 Conclusions

In this study, we examined the seismic velocity variations in response to tides throughout Japan. Utilizing the dense seismic network in Japan, we investigated the spatial extent of the tidal strain–velocity sensitivities. Accordingly, we extracted the tidal responses to velocity variations from the hourly stacked noise autocorrelations by combining the extended Kalman filter with the Maximum Likelihood method. The strain–velocity sensitivities varied from approximately 10^3 to 10^5. Upon comparing the strain–velocity sensitivity with the S-wave velocity structure in Japan, the tidal response to seismic velocity variations was larger at low S-wave velocities in the shallow crust. Based on the strain–velocity relationship in the grain material, the current results implied that the spatial variations in the tidal response of seismic wave velocity can potentially characterize the fluid pressure or shape of pores in the crust. The tidal responses to velocity variations in various time periods were extracted to investigate the temporal variations in the mechanical properties of the shallow crust. Future studies can utilize dense seismic networks such as a Large N-array or DAS observation to attain a higher spatial resolution of tidal strain–velocity sensitivity.

Open Research

We used data from Hi-net (doi.org/10.17598/nied.0003) managed by the National Research Institute for Earth Science and Disaster Prevention (NIED), Japan. The python code of the extended Kalman filter is also available on the Zenodo web page (https://zenodo.org/record/7476091#.Y8_BluzP20p).

Acknowledgments

The authors are grateful to people for maintaining the network and making the data readily available. This work was supported by JSPS KAKENHI Grand Number JP22K14110.

This work made use of ObsPy (Beyreuther et al., 2010), Numpy (Van Der Walt et al., 2011) and SciPy (Virtanen et al., 2020), and GMT programs (Wessel & Smith, 1998).

References

Akaike, H. (1974). A new look at the statistical model identification. *IEEE transactions on automatic control*, *19*(6), 716–723.

Beyreuther, M., Barsch, R., Krischer, L., Megies, T., Behr, Y., & Wassermann, J. (2010). Obspy: A python toolbox for seismology. *Seismological Research Letters*, *81*(3), 530–533.

Brenguier, F., Campillo, M., Hadziioannou, C., Shapiro, N. M., Nadeau, R. M., & Larose, E. (2008). Postseismic relaxation along the san andreas fault at parkfield from continuous seismological observations. *science*, *321*(5895), 1478–1481.

Brenguier, F., Campillo, M., Takeda, T., Aoki, Y., Shapiro, N., Briand, X., ... Miyake, H. (2014). Mapping pressurized volcanic fluids from induced crustal seismic velocity drops. *Science*, *345*(6192), 80–82.

Brenguier, F., Shapiro, N. M., Campillo, M., Ferrazzini, V., Duputel, Z., Coutant, O., & Nercessian, A. (2008). Towards forecasting volcanic eruptions using seismic noise. *Nature Geoscience*, *1*(2), 126–130.

Cartwright, D., & Edden, A. C. (1973). Corrected tables of tidal harmonics. *Geophysical journal international*, *33*(3), 253–264.

De Fazio, T. L., Aki, K., & Alba, J. (1973). Solid earth tide and observed change in the in situ seismic velocity. *Journal of Geophysical Research*, *78*(8), 1319–1322.

Durbin, J., & Koopman, S. J. (2012). *Time series analysis by state space methods* (Vol. 38). OUP Oxford.

Hillers, G., Retailleau, L., Campillo, M., Inbal, A., Ampuero, J.-P., & Nishimura, T. (2015). In situ observations of velocity changes in response to tidal deformation from analysis of the high-frequency ambient wavefield. *Journal of Geophysical Research: Solid Earth*, *120*(1), 210–225.

Hobiger, M., Wegler, U., Shiomi, K., & Nakahara, H. (2014). Single-station cross-correlation analysis of ambient seismic noise: application to stations in the surroundings of the 2008 iwate-miyagi nairiku earthquake. *Geophysical Journal*

International, *198* (1), 90–109.

Maeda, T., Obara, K., Furumura, T., & Saito, T. (2011). Interference of long-period seismic wavefield observed by the dense hi-net array in japan. *Journal of Geophysical Research: Solid Earth*, *116* (B10).

Mao, S., Campillo, M., van der Hilst, R. D., Brenguier, F., Stehly, L., & Hillers, G. (2019). High temporal resolution monitoring of small variations in crustal strain by dense seismic arrays. *Geophysical Research Letters*, *46* (1), 128–137.

Matsumoto, K., Sato, T., Takanezawa, T., & Ooe, M. (2001). Gotic2: A program for computation of oceanic tidal loading effect. *Journal of the Geodetic Society of Japan*, *47* (1), 243–248.

Nagaoka, Y., Nishida, K., Aoki, Y., Takeo, M., & Ohminato, T. (2012). Seismic imaging of magma chamber beneath an active volcano. *Earth and Planetary Science Letters*, *333*, 1–8.

Nakata, T., & Imaizumi, T. (2002). *Digital active fault map of japan.* University of Tokyo Press, Tokyo.

Nishida, K., Kawakatsu, H., & Obara, K. (2008). Three-dimensional crustal s wave velocity structure in japan using microseismic data recorded by hi-net tiltmeters. *Journal of Geophysical Research: Solid Earth*, *113* (B10).

Nishida, K., Mizutani, Y., Ichihara, M., & Aoki, Y. (2020). Time-lapse monitoring of seismic velocity associated with 2011 shinmoe-dake eruption using seismic interferometry: An extended kalman filter approach. *Journal of Geophysical Research: Solid Earth*, *125* (9), e2020JB020180.

Obermann, A., & Hillers, G. (2019). Seismic time-lapse interferometry across scales. In *Advances in geophysics* (Vol. 60, pp. 65–143). Elsevier.

Reasenberg, P., & Aki, K. (1974). A precise, continuous measurement of seismic velocity for monitoring in situ stress. *Journal of Geophysical Research*, *79* (2), 399–406.

Sagiya, T., Miyazaki, S., & Tada, T. (2000). Continuous gps array and present-day crustal deformation of japan. *Pure and applied Geophysics*, *157* (11), 2303–2322.

Sens-Schönfelder, C., & Eulenfeld, T. (2019). Probing the in situ elastic nonlinearity of rocks with earth tides and seismic noise. *Physical review letters*, *122* (13), 138501.

Shapiro, S. A. (2003). Elastic piezosensitivity of porous and fractured rocks. *Geophysics*, *68*(2), 482–486.

Takagi, R., Nishida, K., Aoki, Y., Maeda, T., Masuda, K., Takeo, M., ... Saito, K. (2015). A single bit matters: Coherent noise of seismic data loggers. *Seismological Research Letters*, *86*(3), 901–907.

Takano, T., Nishimura, T., & Nakahara, H. (2017). Seismic velocity changes concentrated at the shallow structure as inferred from correlation analyses of ambient noise during volcano deformation at izu-oshima, japan. *Journal of Geophysical Research: Solid Earth*, *122*(8), 6721–6736.

Takano, T., Nishimura, T., Nakahara, H., Ohta, Y., & Tanaka, S. (2014). Seismic velocity changes caused by the earth tide: Ambient noise correlation analyses of small-array data. *Geophysical Research Letters*, *41*(17), 6131–6136.

Takano, T., Nishimura, T., Nakahara, H., Ueda, H., & Fujita, E. (2019). Sensitivity of seismic velocity changes to the tidal strain at different lapse times: Data analyses of a small seismic array at izu-oshima volcano. *Journal of Geophysical Research: Solid Earth*, *124*(3), 3011–3023.

Takei, Y. (2002). Effect of pore geometry on vp/vs: From equilibrium geometry to crack. *Journal of Geophysical Research: Solid Earth*, *107*(B2), ECV–6.

Van Der Walt, S., Colbert, S. C., & Varoquaux, G. (2011). The numpy array: a structure for efficient numerical computation. *Computing in science & engineering*, *13*(2), 22–30.

Virtanen, P., Gommers, R., Oliphant, T. E., Haberland, M., Reddy, T., Cournapeau, D., ... others (2020). Scipy 1.0: fundamental algorithms for scientific computing in python. *Nature methods*, *17*(3), 261–272.

Walsh, J. (1965). The effect of cracks on the uniaxial elastic compression of rocks. *Journal of Geophysical Research*, *70*(2), 399–411.

Weaver, R. L., & Lobkis, O. I. (2000). Temperature dependence of diffuse field phase. *Ultrasonics*, *38*(1-8), 491–494.

Wessel, P., & Smith, W. H. (1998). New, improved version of generic mapping tools released. *Eos, Transactions American Geophysical Union*, *79*(47), 579–579.

Yamamura, K., Sano, O., Utada, H., Takei, Y., Nakao, S., & Fukao, Y. (2003). Long-term observation of in situ seismic velocity and attenuation. *Journal of Geophysical Research: Solid Earth*, *108*(B6).

Zhu, C., Byrd, R. H., Lu, P., & Nocedal, J. (1997). Algorithm 778: L-bfgs-b: Fortran subroutines for large-scale bound-constrained optimization. *ACM Transactions on mathematical software (TOMS)*, *23*(4), 550–560.

Supporting Information for "Tidal strain response of seismic wave velocity at shallow crust in Japan"

Tomoya Takano[1] and Kiwamu Nishida[2]

[1]Graduate School of Science and Technology, Hirosaki University

[2]Earthquake Research Institute, the University of Tokyo

Contents of this file

1. Text S1 to S4
2. Figures S1 to S2

Introduction

This supporting information contains information on the detail of the state-space model used in this study, the validation of a prior data covariance, the frequency distribution of the velocity change, and the phase delay of velocity changes to the tides.

Text S1. The state vector $\boldsymbol{\alpha}_t$ and the data vector $\boldsymbol{y}_t^p$ for a pth component of correlations ϕ_t^p are defined by,

$$\boldsymbol{\alpha}_t \equiv \begin{pmatrix} A_t \\ \gamma_t \end{pmatrix}, \boldsymbol{y}_t^p \equiv \begin{pmatrix} \phi_t^p(\tau_s) \\ \vdots \\ \phi_t^p(\tau_e) \end{pmatrix}, \tag{1}$$

where τ_s is the start of lag time and τ_e is the end of lag time. This study used the lag time from 2 to 15 seconds. $\boldsymbol{R}_t$ is an explanatory variables related to a seismic velocity change caused by the tides. $\boldsymbol{H}_t$ is a diagonal matrix:

$$\boldsymbol{H}_t \equiv h_0 \boldsymbol{I}, \tag{2}$$

where h_0 is a prior data covariance and $\boldsymbol{I}$ is an identity matrix. $\boldsymbol{Q}_t$ also can be written as a diagonal matrix:

$$\boldsymbol{Q}_t \equiv \begin{pmatrix} q_0 & 0 \\ 0 & q_1 \end{pmatrix}, \tag{3}$$

where p_0 and p_1 are a prior model covariance of the amplitude of correlations and stretching parameters, respectively.

Text S2.

The sum of squared residuals between reference and observed noise correlations is not necessarily an appropriate data covariance for the Kalman filter because the model covariance also affects the residual. One possible approach is to estimate h_0 as one of the hyper–parameters by the Maximum Likelihood method. However, it is difficult to stably estimate all hyper-parameters at the same time. We thus first determined p_0, p_1, γ_1, A_{M2}, and ϕ_{M2} by the Maximum Likelihood method with the sum of squared residuals as h_0. By using the determined parameters, we then searched an optimal h_0 by the Maximum Likelihood method with the sum of squared residuals as the initial value of h_0. The estimated h_0 was used to re-determine p_0, p_1, γ_1, A_{M2}, and ϕ_{M2}. Figure S1 shows the logarithmic likelihood as a function of the normalized hyper–parameters with different data covariance. The results were not much different from the hyper–parameters estimated with the sum of squared residuals as data covariance, which is consistent with the consideration of misfit function with unknown data covariance (Dosso & Wilmut, 2006). Therefore, this study used the sum of squared residuals between reference and observed correlations as data covariance.

Text S3.

Figure S2 shows the frequency distribution of the velocity change at the station where ΔAIC is smaller than 0 and Δ AIC is larger than 0, respectively. At stations where Δ AIC is greater than 0, the velocity change is generally estimated to be smaller than 0.001 %, indicating the tidal response of velocity changes is not statistically significant.

Text S4.

We mapped the phase delay of the seismic velocity variations with respect to the tidal strain (Figure 3 (c)). The phase delay of the velocity variations to the applied strain was potentially caused by the nonlinear elastic response of the rocks (Sens-Schönfelder & Eulenfeld, 2019), such as hysteresis in the rock (Guyer et al., 1995) or slow dynamic recovery after dynamic perturbations (Ostrovsky & Johnson, 2001). The majority of the phase differences observed in this study were approximately 0°. In certain stations, the phase shift reached up to approximately 3 h. The magnitude of this phase shift was consistent with the seismic velocity variations observed in response to the tidal strain with heterogeneous gypcrete in Chile (Sens-Schönfelder & Eulenfeld, 2019). Moreover, several stations exhibited a phase shift of approximately 180°. A phase shift of 180° indicated that the seismic velocity decreased and increased during the contraction and dilatation of the medium, respectively. Although the negative strain–velocity sensitivity can be explained based on the localized fluid movement in the shallow regions owing to tides, the occurrence of such fluid movement could not be verified. Certain stations exhibited negative phase shifts as well, indicating that the velocity variations delayed the tidal deformation shift by more than 12 h or the velocity variations occurred prior to the deformation. Note that the phase must be off by more than 180 degrees to satisfy causality. Although this study analyzed only the volumetric strain, the orientation of the cracks may govern their strain response in certain directions. In this regard, few studies have discussed the phase delay of velocity variations with respect to the deformation, and the phase lag occurring at the crustal-scale is under discussion. To clarify the phase shifts of the velocity variations with respect to the applied strain, the phase shift mechanisms should be further investigated considering fluid movement and strain orientations.

References

Dosso, S. E., & Wilmut, M. J. (2006). Data uncertainty estimation in matched-field geoacoustic inversion. *IEEE Journal of Oceanic Engineering*, *31*(2), 470–479.

Guyer, R., McCall, K., & Boitnott, G. (1995). Hysteresis, discrete memory, and nonlinear wave propagation in rock: A new paradigm. *Physical review letters*, *74*(17), 3491.

Ostrovsky, L., & Johnson, P. A. (2001). Dynamic nonlinear elasticity in geomaterials. *La Rivista del Nuovo Cimento*, *24*(7), 1–46.

Sens-Schönfelder, C., & Eulenfeld, T. (2019). Probing the in situ elastic nonlinearity of rocks with earth tides and seismic noise. *Physical review letters*, *122*(13), 138501.

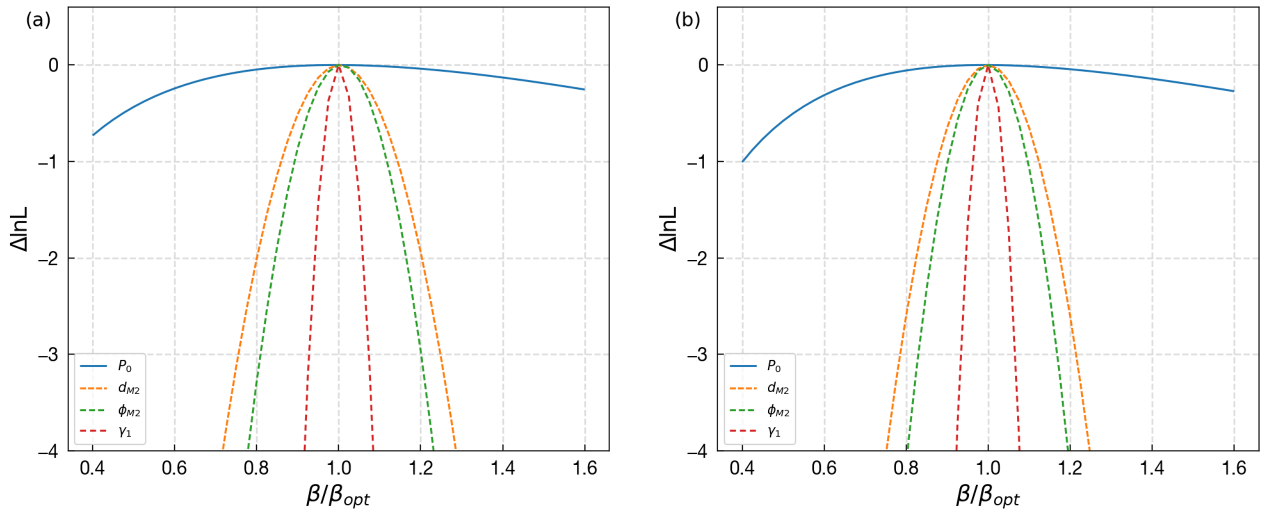

Figure S1. The logarithmic likelihood as a function of the normalized hyper–parameters with the data covariance estimated by the sum of the squared residual between reference and observed correlations (a) and the data covariance estimated by the Maximum likelihood method (b).

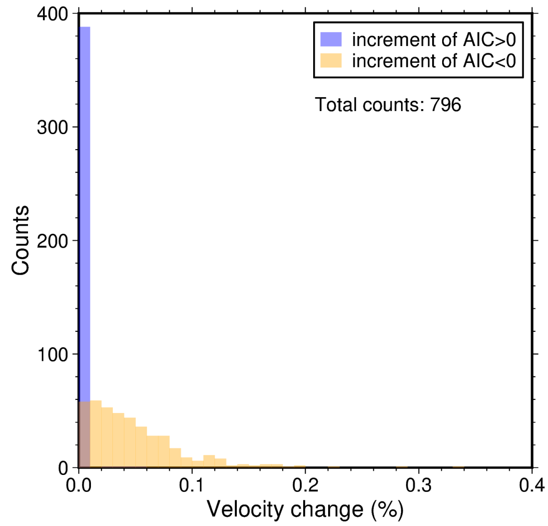

Figure S2. The frequency distribution of velocity changes. Blue bar shows the velocity changes at the stations with increments of AIC larger than 0. Orange bar shows the velocity changes at the stations with increments of AIC smaller than 0.